

Research paper

New families of triply periodic minimal surface-like shell lattices

Yonglai Xu ^a, Hao Pan ^b, Ruonan Wang ^c, Qiang Du ^d, Lin Lu ^{a,*}^a School of Computer Science and Technology, Shandong University, 72 Binhai Road, Qingdao, 266237, China^b Microsoft Research Asia, 5 Danling Road, Beijing, 100080, China^c Faculty of Engineering and Physical Sciences, University of Surrey, Surrey GU2 7XH, Guildford, UK^d Institute of Engineering Thermophysics, Chinese Academy of Sciences, Haidian District, Beijing, 100190, China

ARTICLE INFO

Keywords:

Triply periodic minimal surfaces

Shell lattices

Microstructures

Mechanical properties

ABSTRACT

Triply periodic minimal surface (TPMS)-based shell lattices are increasingly recognized for their exceptional geometric and mechanical attributes. Their open-cell configuration further establishes them as prime candidates for additive manufacturing, especially using liquid-bath or powder-bed techniques. While TPMS can be developed through both implicit and explicit methods, each has its limitations. Implicit methods, commonly adopted, are constrained by a limited set of known functions and a singular level set parameter, narrowing the modeling space. On the other hand, explicit methods, though they aim to minimize the surface area functional, encounter challenges in generating surfaces of high genus due to the complexity in achieving specific topologies. In this paper, we unveil a novel modeling approach for TPMS-like shell lattices. Central to our approach is the creation of periodic boundaries that seamlessly integrate implicitly formed complex surface patches. Our methodology introduces a parametric representation for these boundaries, leveraging a unique search algorithm paired with spline curve parameterization. Following this, we implement a formulation of geometric currents harmonized with boundary periodicity C^1 continuity to determine the associated TPMS. This innovation spawns a variety of parametric TPMS-like shell-lattice topologies. Using the homogenization method, we assess the elastic attributes of these diverse families. Our findings reveal that the mechanical property spectrum of our TPMS-like shell lattices surpasses that of conventional TPMS-based counterparts. We spotlight two applications for our modeling technique: designing functionally graded materials and implementing inverse homogenization. Concluding our study, we validate our innovations through a sequence of empirical tests.

1. Introduction

With advances in manufacturing engineering, lightweight yet high-strength sophisticated porous structures based on shell-lattices have gained prominence, finding applications in numerous engineered systems [1,2]. Among shell-lattices, the triply periodic minimal surface (TPMS)-based shell-lattices stand out as captivating microstructures. Their appeal stems from their smoothness, complete connectivity, and open-cell topology. A TPMS is a unique minimal surface that manifests periodicity in three orthogonal directions, effectively dividing space into two continuous, non-overlapping subspaces. Their exceptional geometric qualities play a pivotal role in their application efficacy. For instance, TPMS-based shell-lattices consistently showcase remarkable mechanical resilience at reduced relative densities [3]. They mitigate stress concentration more effectively than truss-lattices [4] and offer

manufacturing benefits over plate-lattices [5]. The versatility of TPMS structures is further evidenced by their application in domains such as heat exchangers [6,7], biomedical implants [8], tissue engineering scaffolds [9,10], lightweight frameworks [2], and acoustic absorbers [11]. They also hold potential in membrane technologies [12] and enhancing electrical conductivities [13]. Intriguingly, nature too exhibits structures reminiscent of TPMS, underscoring their potential in biomimetic designs [14,15].

The construction of TPMS-based shell-lattices has gained considerable attention. TPMS can be generated using implicit methods or explicit methods, which have different strengths in modeling flexibility. In the implicit method, the TPMS can be described by a single-valued function of three variables consisting of trigonometric functions. Take three classical TPMS units (P, D, G) as examples, these surfaces can be described approximately by the zero-level value of the following level

* Corresponding author.

E-mail address: llu@sdu.edu.cn (L. Lu).

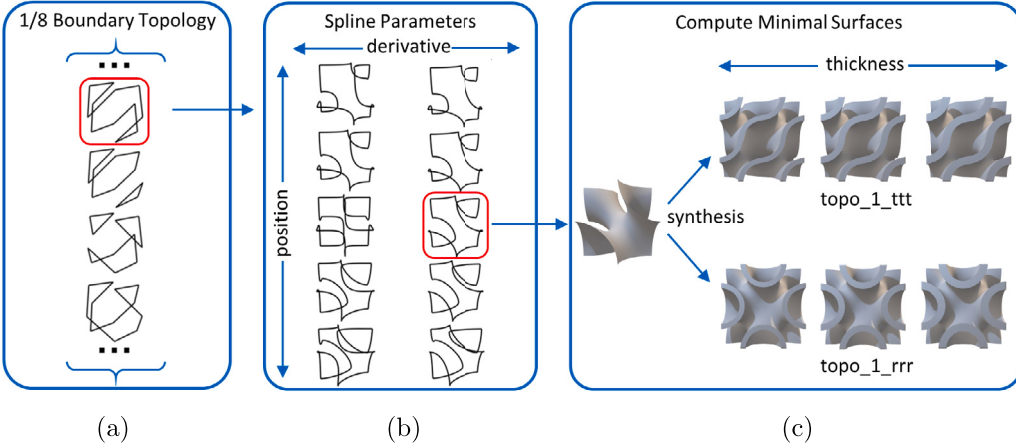


Fig. 1. Overview of our TPMS shell lattice modeling framework. We first define the boundary curve for a 1/8 lattice cube, which consists of two steps: (a) topology enumeration and (b) geometry variation. Given the boundary curve, (c) we use implicit method to compute for the adapted minimal surface with boundary continuity.

set equations, respectively:

$$\begin{aligned}\phi_P(x, y, z) &= \cos(x) + \cos(y) + \cos(z) = c \\ \phi_D(x, y, z) &= \cos(x)\cos(y)\cos(z) - \sin(x)\sin(y)\sin(z) = c \\ \phi_G(x, y, z) &= \sin(x)\cos(y) + \sin(z)\cos(x) + \sin(y)\cos(z) = c\end{aligned}\quad (1)$$

The discrete mesh model of zero surface can conveniently be extracted based on the well-known marching cube algorithm [16]. Due to the efficiency of the implicit method, all the applications described above preferred this form in the construction of TPMS-based shell-lattices. However, implicit functions are known only for a few TPMS structures, and the geometry of TPMS can have variations only by adjusting the single parameter c , which limits the modeling ability for TPMS. In explicit methods, an explicitly constructed surface patch is evolved iteratively by minimizing surface area, subject to the boundary constraints that ensure the periodic compositionality of patches. Therefore, the challenge with explicit methods lies in balancing the boundary flexibility for triply periodic composition and the explicit surface patch computation for given boundaries. Indeed, existing works mostly construct TPMS patches bounded inside cells of crystallographic symmetries, where the periodicity is guaranteed and the individual patches are simple enough to compute explicitly. For example, Schwarz and Neovius explored the first 5 TPMS examples [17]. [18] found 12 new TPMS derived from the Schwarz surfaces and have fundamental patches bounded within kaleidoscopic cells of reflection symmetry. [19] studies TPMS supported by crystalline lattices where the fundamental patches are bounded by straight lines and naturally composed through 180° rotations along the boundary lines. [20] develops the conjugate surface algorithm to convert between patches bounded by free boundaries or straight lines and the method of handle insertion, which further enriches the TPMS class. While such procedures classify TPMS structures under specified construction symmetries, the fundamental patches assume fully specified simple topology, as explicit patches have difficulty modeling changing or complex topology.

In this work, we propose a new framework for modeling TPMS shell lattices with enhanced flexibility. Our approach combines the advantages of both implicit methods and explicit methods, by explicitly specifying flexible periodic boundaries and implicitly computing minimal surfaces adhering to the boundaries. Specifically, we build on the technology of [21,22] that uses geometric measure theory to find minimal surfaces of changing topologies implicitly, which allows us to design complex boundary conditions in a much more flexible manner than traditional explicit methods mentioned above.

Our framework consists of two major components (Fig. 1). The first component addresses the main challenge of constructing periodic boundaries. A key insight is to split a periodic unit cell into 1/8

cubes and construct boundaries there, which on one hand simplifies the construction of boundary conditions and makes implicit minimal surface patch computation robust, and on the other hand provides sufficient complexity by combining 1/8 cubes into a unit cell. Given the boundaries, the second component of our framework is to compute smooth minimal surfaces fitting to the boundaries by extending the implicit methods of [21,22]. In particular, smoothness at the boundary is critical when we synthesize the resulting minimal surfaces, which we ensure by extending the implicit method with smoothness constraints.

Utilizing our computational approach, we have identified new categories of TPMS-like shell lattices with varied structures. When juxtaposed with existing TPMS shell-lattices, our findings indicate that our shell-lattices can expand the material property spectrum (specifically, Young's modulus and Poisson's ratio). Additionally, they enhance the surface area-to-volume ratio and achieve isotropic stiffness. These attributes present significant and novel alternatives for microstructure material engineering. In terms of applications, our parametric boundary model facilitates the establishment of a bidirectional mapping between geometric parameters and mechanical properties using neural networks. Furthermore, by anchoring the outer boundary parameters, we can design functionally graded structures that boast impeccable connectivity. We substantiate these findings and their practical applications with examples and data analysis.

2. Methods

Our methodology for modeling TPMS-based shell-lattices consists of two main stages (Fig. 1). We first introduce the explicit construction of periodic boundaries, which includes the choice of 1/8 cube for boundary construction (Section 2.1), the search of boundary topology that guarantees triple periodicity and boundary shape parameterization (Section 2.2). Then we solve for corresponding TPMS implicitly, by an adapted formulation of geometric currents with boundary C^1 continuity constraint to guarantee the smoothness and high mesh quality at the boundary (Section 2.3).

2.1. 1/8 Cube cell

Among all crystallographic symmetries, cube decomposition provides a simple unit for constructing triply periodic surfaces, as given a surface patch with suitable periodicity boundaries inside the cube, a larger TPMS can be trivially constructed by tiling the basic patch along three axes. However, in this work, we propose to work with the 1/8 unit cube instead, which achieves both computational robustness and modeling flexibility.

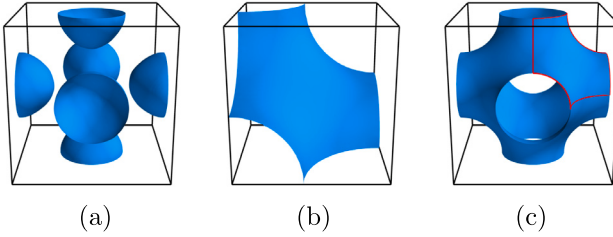


Fig. 2. Using 1/8 cube for robust and flexible TPMS generation. (a) On a unit cube the minimal surface with six circular boundaries degenerates to disconnected components. Minimal surfaces are local minima of surface area and are more likely to degenerate under more complex boundary conditions that admit multiple solutions. In contrast, (b) the minimal surface can be generated successfully on a 1/8 cube with boundary condition trimmed from the unit cube. (c) the surface of (b) can then be composed back onto the unit cube as a high-genus connected surface.

The boundaries on a unit cube can be a single closed curve or multiple closed curves as long as they comply with triple-periodicity constraints. By restricting to single closed boundaries, the boundary topology variations are limited. In contrast, multiple closed boundaries enable more flexible boundary topologies. However, they are also more likely to result in the degeneracy of minimal surfaces (Fig. 2(a)), which breaks the connectivity of structures. The reason for degeneracy is that minimal surfaces are local optimal solutions of surface area minimization. For larger patches with very complex boundaries, there can be more local minimum, among which a numerical method is more likely to miss the interesting ones and lock onto degenerate solutions. On the other hand, by restricting to 1/8 cube cells, there are multiple benefits. First, we can decrease the search space complexity by focusing on simpler boundary curves, while the composition of 1/8 cells into a unit cell still allows for very complex boundaries and topologies. Second, within a simpler 1/8 cell, the minimal surface patch has fewer local minima and can be more robustly constructed. As shown through the example of Fig. 2(b)(c), by working with 1/8 cell, a properly connected TPMS with the same boundary as Fig. 2(a) can be found.

2.2. Boundary construction

To fully explore the space of possible boundaries, we divide the task into two subtasks: *topology enumeration* and *geometric variation*.

Boundary topology enumeration. Assuming that the boundary is free from self-intersection, we can systematically explore the space of admissible boundary topologies by representing them as graphs. In this graph representation, each node corresponds to an intersection point between the boundary curve and a cube edge, while each edge represents a simplified intersection between the boundary curve and a cube face (refer to Fig. 5). As illustrated in Fig. 3, there are eight possible connections for the edge nodes on each face. Consequently, the total number of potential topologies that traverse all six faces amounts to 8^6 , subject to further constraints. The constraints are applied as follows. First, since boundary curves are closed, the degree (i.e. the number of adjacent edges) [23] of each node should be either 2 or 0, which reduces the number of topologies dramatically to 256. Fig. 4(a) illustrates a non-closed topology with nodes having a degree of 1. Second, some topologies are equivalent under the cubic symmetries of rotation and reflection. For example, Fig. 4(b)(c)(d) depict closed topologies that are equivalent under cubic symmetry. After eliminating these duplicates, there are a total of 20 unique topologies, all of which are presented in Fig. 5. It can be found that only topo_1, topo_3 and topo_6 are triply periodic topologies.

To synthesize the 1/8 cell boundary topology to a unit-cell with triple periodicity, we can use two symmetrical relationships along an axis: translation and reflection. Different symmetries along each axis impose different requirements on the admissible 1/8 topology.

Translation symmetry requires that the boundary on opposite faces are congruent, while reflection symmetry has no constraints. For example, the boundary topology of topo_19 synthesized by three reflections and topo_1 synthesized by three translations are shown in Fig. 11(a) and (b), respectively. It is worth noting that the boundary topology shown in Fig. 11(a) consists of multiple closed boundaries, but it is constructed from the single closed boundary topo_19.

For convenience of discussion, we denote the topology of a unit cell as topo_id_x₁x₂x₃, where id specifies the 1/8 topology listed in Fig. 5, and x₁x₂x₃, x ∈ {r, t} gives the synthesis symmetry (r for reflection, t for translation) along three axes, respectively. In summary, if we design the boundaries on the entire cube we can only get three triply periodic topologies. But we can greatly increase the number of triply periodic topologies by combining the 1/8 topology and the synthetic way.

Boundary geometric variation. To construct concrete boundary curves for each topology, we convert each edge in the topology graph into cubic Hermite splines [24], which facilitates the generation of geometric variations. A cubic Hermite spline curve is fully determined by four parameters [25]: the starting point of the curve (p_1), the direction in which the curve leaves the starting point (d_1), the endpoint of the curve (p_2), and the direction in which the curve leaves the endpoint (d_2). Assuming a cubic polynomial function $P(x) = C_0 + C_1x + C_2x^2 + C_3x^3$, we can compute the values of C_0, C_1, C_2 , and C_3 by solving the following equations:

$$\begin{cases} p_1 = P(0) = C_0 \\ p_2 = P(1) = C_0 + C_1 + C_2 + C_3 \\ d_1 = P'(0) = C_1 \\ d_2 = P'(1) = C_1 + 2C_2 + 3C_3 \end{cases} \quad (2)$$

So we assign three parameters for each topology node: position, incident derivative and emergent derivative. When generating variations, the position of a node is changed while being constrained to the cube edge where it is located, and the derivatives are varied while being constrained to stay on the cube faces. Fig. 6 shows two geometric variations for topo_1 and topo_19, respectively.

2.3. Computing minimal surfaces

Given any boundary generated in the above way, we can compute the corresponding minimal surface bordered by this boundary using the implicit method of [22], which requires no specified initial surface and can freely change interior topology. In Fig. 7, we present two examples demonstrating the process of minimal surface computation. The figure showcases the resulting geometric shapes at different iteration stages.

However, the resulting minimal surfaces, when tiled in space, may not be C^1 continuous at the boundary. In addition, due to the limited accuracy of implicit representation by neural networks, the mesh quality extracted by the marching cubes algorithm is poor at the boundary, as shown in Fig. 8. Such non-smoothness and irregularity are undesirable, as they will produce discontinuous mechanical properties that cause stress concentration at the boundary.

To alleviate these problems, we extend the formulation of [22] to ensure C^1 continuity across boundary. In [22], a surface is represented implicitly by the zero-level set of a function f_θ , which is implemented by neural network with trainable weights θ , and surface boundary Γ is represented explicitly by polygonal curves. Based on geometric measure theory, the computation of minimal surface is solved as a minimal mass problem:

$$\arg \min_{\theta} E_{x \sim U} [|\nabla_x f_\theta(x) + \alpha_\Gamma^\#(x)|] \quad (3)$$

where $\nabla_x f_\theta(x)$ is the gradient of f at point x uniformly sampled in the 1/8 cube domain U , and $\alpha_\Gamma^\#(x)$ defines the Biot–Savart field that physically models the magnetic field generated by constant electric current

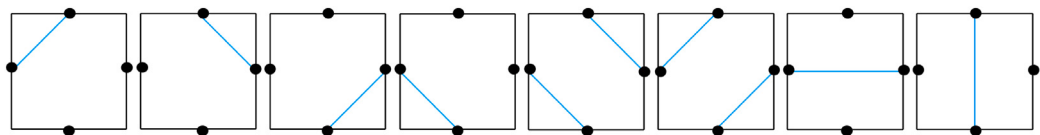


Fig. 3. Boundary topologies on a cube face. Treating the cube edges as nodes, we can enumerate the 8 possible boundary curve topologies that pass through a face.

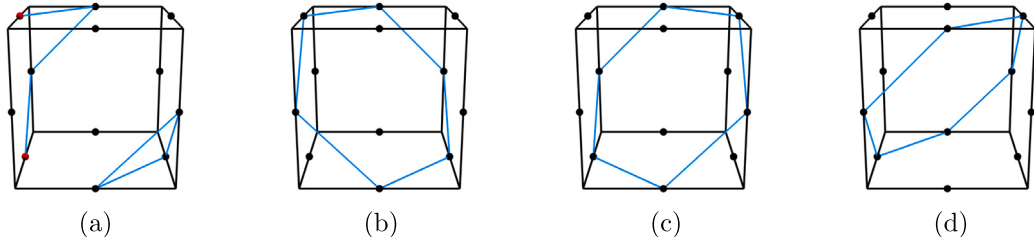


Fig. 4. Filtering non-closed or redundant boundary topologies. (a) is a non-closed topology because of the nodes having a degree of 1 (marked in red). (b-d) are of the same topology under appropriate symmetry transformations: (b) to (c) by left-right reflection and (b) to (d) by rotation around the horizontal axis.

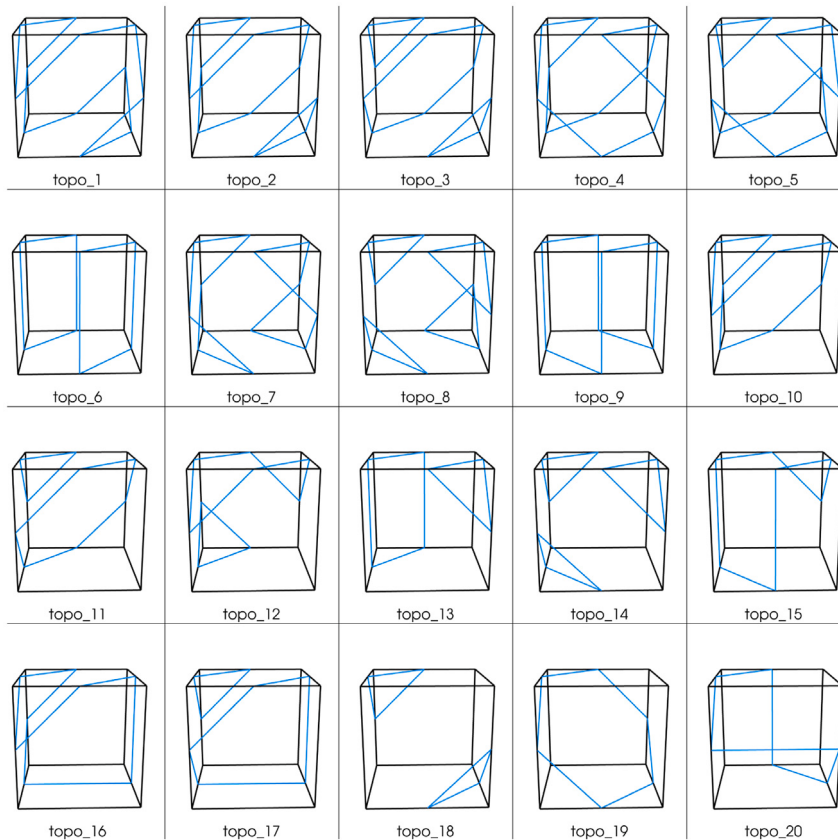


Fig. 5. The 20 unique boundary curve topologies for a 1/8 cube.

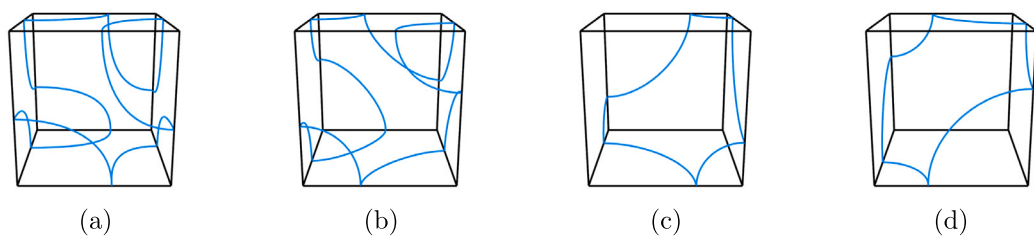


Fig. 6. Geometric variations of boundary curves can be generated by changing node position and derivative parameters. (a)(b) have topo_1 and (c)(d) have topo_19.

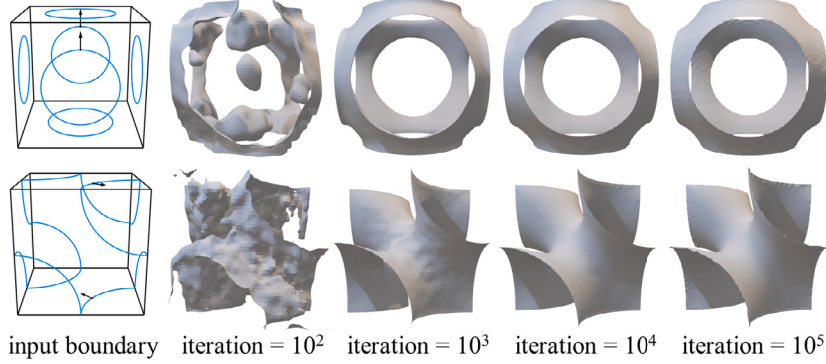


Fig. 7. The geometry variation process in the process of computing minimal surfaces.

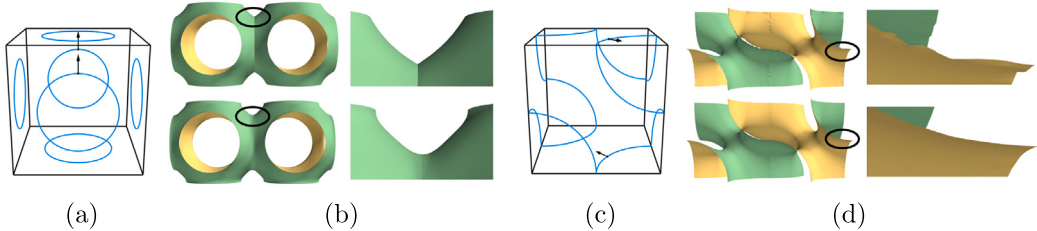


Fig. 8. Surface smoothness at boundary curves. The smoothness and surface regularity at boundary are largely improved after adding C^1 continuity constraint. (a)(c) show the input boundary curves and arrows indicating the surface normal directions at specified points. (b)(d) show the minimal surfaces without boundary constraints (top row) and with boundary constraints (bottom row), with zoom-ins at the circled regions to highlight the surface details.

flowing through the boundary curves [22]. The network weights θ are optimized by simple stochastic gradient descent to convergence.

We apply surface continuity constraints for boundary parts with two symmetry types (i.e., translation, reflection) accordingly.

For boundary part $\Gamma_t \subset \Gamma$ subject to translation symmetry, the gradients of boundary point p_{bdry} and its symmetric point \bar{p}_{bdry} at opposite face have equal magnitude, and their directions are the same (Fig. 8(a)) or opposite (Fig. 8(c)), depending on whether the orientation of the surface changes between the two boundary parts. Thus we add the following E_t to Eq. (3):

$$E_t = \sum_{p_{bdry} \in \Gamma_t} |\nabla_{p_{bdry}} f_\theta(p_{bdry}) \pm \nabla_{\bar{p}_{bdry}} f_\theta(\bar{p}_{bdry})| \quad (4)$$

where - is used for the same direction gradients and + is used for opposite direction gradients instead.

For boundary part $\Gamma_r \subset \Gamma$ subject to reflection symmetry, we only constrain the directions of gradients of every boundary point to be perpendicular to the corresponding axis:

$$E_r = \sum_{p_{bdry} \in \Gamma_r} |\nabla_{p_{bdry}} f_\theta(p_{bdry}) \cdot \vec{a}_{p_{bdry}}| \quad (5)$$

For example, the E_r term for boundary points located at the cube faces, which are perpendicular to x -axis, has $\vec{a} = (1, 0, 0)$.

As shown in Fig. 8, with the boundary constraint loss terms, the surface smoothness and regularity at the boundary are largely improved.

Remark. By incorporating surface tangential constraints on specified boundary curves, we solve a more constrained variant of the Plateau's problem: the optimized surfaces strike a balance between pure surface area minimization and boundary smoothness, and therefore approximate minimal surfaces. We name the structures we find as TPMS-like shell lattices. Approximate TPMS structures are highly useful for microstructure material design, as shown by the widespread usage of the various implicit function based approximations given by Eq. (1). In Section 3 and Fig. 15, we show that our TPMS-like surfaces are high quality approximations of minimal surfaces as good as commonly used TPMS surfaces.

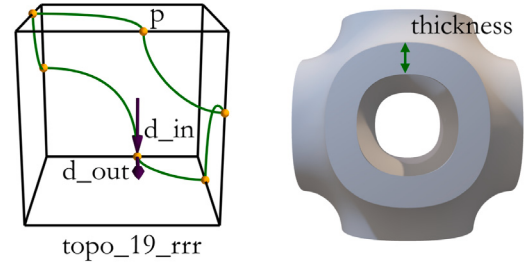


Fig. 9. The parametric representation of shell structures. topo_19_rrr represents the unit topology. P represents node position parameter. d_{in} and d_{out} represent the incident derivative and emergent derivative of node, respectively.

2.4. Shell construction

We obtain solid shell structures by extruding the smooth surface along local normal vectors bidirectionally. We use different thickness parameters to generate solid shell structures with different relative densities. We can use a unified parametric representation to represent each structure. The parameters include topology type, boundary parameters (node position P and node derivative d), and structure thickness t . Take the shell structures in Fig. 9 as an example; this model can be represented by one thickness and topology type parameters, six position parameters, and twelve derivative parameters.

3. Results

In this section, we first show various shell-lattices generated by the proposed method. Then the space of mechanical properties (Young's modulus E and Poisson's ratio ν), which can achieve for our shell-lattices and TPMS-based shell-lattices in the same relative density, are shown for comparison. The isotropy and surface area to volume ratio (SA/V ratio) are also analyzed. Physical experiments are shown to validate the conclusions drawn from numerical simulations.

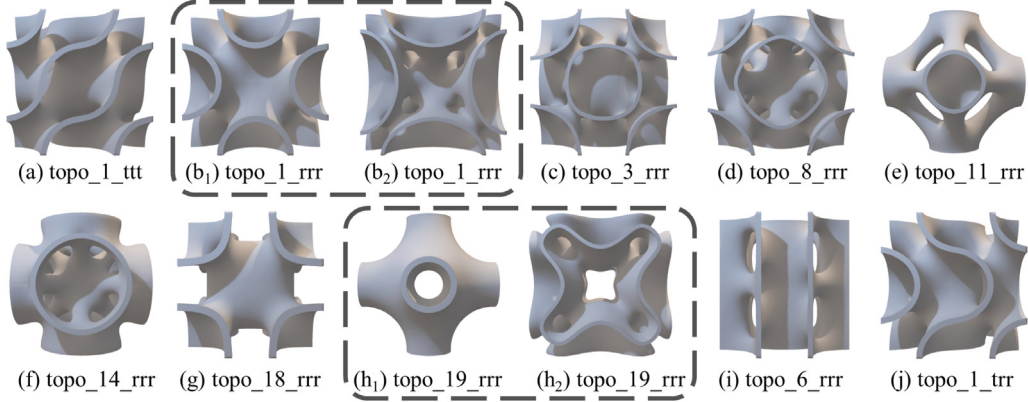


Fig. 10. Some shell-lattices generated by our method. There are large variations in both topology and geometry. (b)–(h) are cubic symmetric structures, (b)–(i) are orthotropic structures, (a) and (j) are anisotropic structures.

3.1. Analysis of TPMS-like structures

Diverse TPMS shells with vastly different geometry, topology and therefore material properties can be constructed with our method. Examples are shown in Fig. 10, where we use different 1/8 cube topologies (see Fig. 5) and ways of composition to construct ten different unit cube topologies; topology variations of inner surface induced by different nodal parameters are also shown in (b₁)(b₂) and (h₁)(h₂) for topo_1_rrr and topo_19_rrr, respectively. The material properties can be assessed based on the characteristics of the stiffness matrix calculated through homogenization [26,27]. We note that unit structures constructed by three reflections are always orthotropic due to the symmetries along the three axes, as depicted in (b)–(i). On the other hand, translation can lead to anisotropic structures, as shown in (a) and (j). Furthermore, due to the congruent geometry specified along the axis directions, (b)–(h) are cubic symmetric structures [28], i.e., each of them has the same material properties along three axes. Although the structure (a) is anisotropic, it is special because the nodal points of topo_1_ttt always coincide with edge midpoints. Consequently, its material properties are also equivalent along all three axes. We will verify this property through physical experiments in Section 3.2.

To assess the mechanical properties of various structures, we employ the numerical homogenization method as detailed in [29]. We discretize the unit cube using a regular $60 \times 60 \times 60$ grid. The base material in the homogenization is defined with a Young's modulus of 1 MPa and a Poisson's ratio of 0.3. For metamaterial architectures with cubic symmetry, the linear elastic stress{ σ }-strain{ ϵ } relationship can be expressed as:

$$\begin{Bmatrix} \sigma_{11} \\ \sigma_{22} \\ \sigma_{33} \\ \sigma_{23} \\ \sigma_{31} \\ \sigma_{12} \end{Bmatrix} = \begin{bmatrix} C_{11} & C_{12} & C_{12} & 0 & 0 & 0 \\ C_{12} & C_{11} & C_{12} & 0 & 0 & 0 \\ C_{12} & C_{12} & C_{11} & 0 & 0 & 0 \\ 0 & 0 & 0 & C_{44} & 0 & 0 \\ 0 & 0 & 0 & 0 & C_{44} & 0 \\ 0 & 0 & 0 & 0 & 0 & C_{44} \end{bmatrix} \begin{Bmatrix} \epsilon_{11} \\ \epsilon_{22} \\ \epsilon_{33} \\ \epsilon_{23} \\ \epsilon_{31} \\ \epsilon_{12} \end{Bmatrix} \quad (6)$$

According to the stiffness matrix C , we can compute Young's modulus E , Poisson's ratio ν , shear modulus G and Zener's anisotropy ratio Z that evaluates the anisotropy properties [30] in all directions, as follows:

$$E = (C_{11}^2 + C_{12}C_{11} - 2C_{12}^2)/(C_{11} + C_{12}) \quad (7)$$

$$\nu = C_{12}/(C_{11} + C_{12}) \quad (8)$$

$$G = C_{44} \quad (9)$$

$$Z = 2C_{44}/(C_{11} - C_{12}) \quad (10)$$

For comparison, we choose shell-lattices which resemble prior TPMS-based shell-lattices based on the similarity of outer boundary topology of unit cell. Five types of outer boundary topologies of TPMS, including Schwarz Primitive (P), Schwarz Diamond (D), Schoen's I-WP (IWP), Schoen's F-RD (FRD) and Neovius (N) are shown in Fig. 11. We assign specific names to our structures based on their corresponding boundary conditions. The P-like structures encompass topo_11_rrr, topo_14_rrr and topo_19_rrr. The D-like structures consist of topo_1_ttt. The IWP-like structures include topo_18_rrr. The FRD-like structures encompass topo_3_rrr and topo_8_rrr. Lastly, the N-like structures consist of topo_1_rrr.

We compare the mechanical properties (Young's modulus E and Poisson's ratio ν) for both our shell-lattices and the corresponding prior TPMS shell-lattices. To generate our shell-lattices, we employ various parameters. For TPMS-based structures, we extract solid TPMS models using two different iso-surfaces, denoted as c_1 and c_2 . By enumerating different values of c_1 and c_2 , we can generate a series of solid TPMS models [31]. The relative densities of all structures generated are fixed at 0.3 (the error is controlled within 0.01). The E - ν space covered by our shell-lattices and prior TPMS-based shell-lattices are shown in Fig. 12. The theoretical Hashin-Shtrikman bound (H-S bound) [32] for isotropic stiffness under 0.3 volume fraction is plotted in a red dashed line. We can see that the difference in E - ν space between our structures and prior TPMS-based structures for every group is significant. The total E - ν space covered by our structures have a larger area compared with prior TPMS-based structures. Further, for our P-like and N-like shell-lattices, the Young's modulus space covered by them are larger than by P and N shell-lattices. N-like shell-lattices cover the largest range of Young's modulus in these structures. IWP-like shell-lattices can exhibit larger Young's modulus compared with IWP shell-lattices and it is closest to the H-S bound in these structures.

Two reasons explain that our structures have a larger coverage area in E - ν space compared with prior TPMS-based shell-lattices. On the one hand, changing our boundary parameters can provide richer shapes than just adjusting the parameter c of the TPMS implicit equations. For example, Fig. 13, the first row shows a group of N surfaces by changing c values, and the second row is a group of N-like surfaces by changing boundary parameters. It is obvious that our group has richer shape variations. On the other hand, the resulting surfaces generated by our different topologies in Fig. 5 can have the same outer boundary topology but different inner architectures after being composed into a unit cell. For example, Fig. 10 shows that two different shell-lattices (c) and (d) with similar outer boundary topology are generated by topo_3_rrr, topo_8_rrr, and shell-lattices (e) and (h1) are generated by topo_11_rrr and topo_19_rrr. Given the same outer boundary topology, richer interior topological and geometric variations enable covering a large scope of mechanical properties.

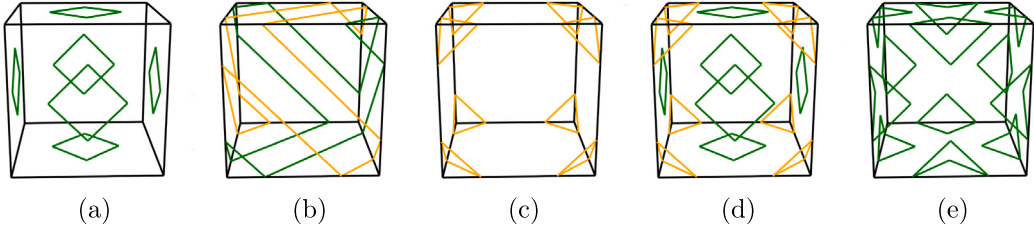


Fig. 11. Five types of outer boundary topologies of (a) Schwarz Primitive, (b) Schwarz Diamond, (c) Schoen's I-WP, (d) Schoen's F-RD, and (e) Neovius.

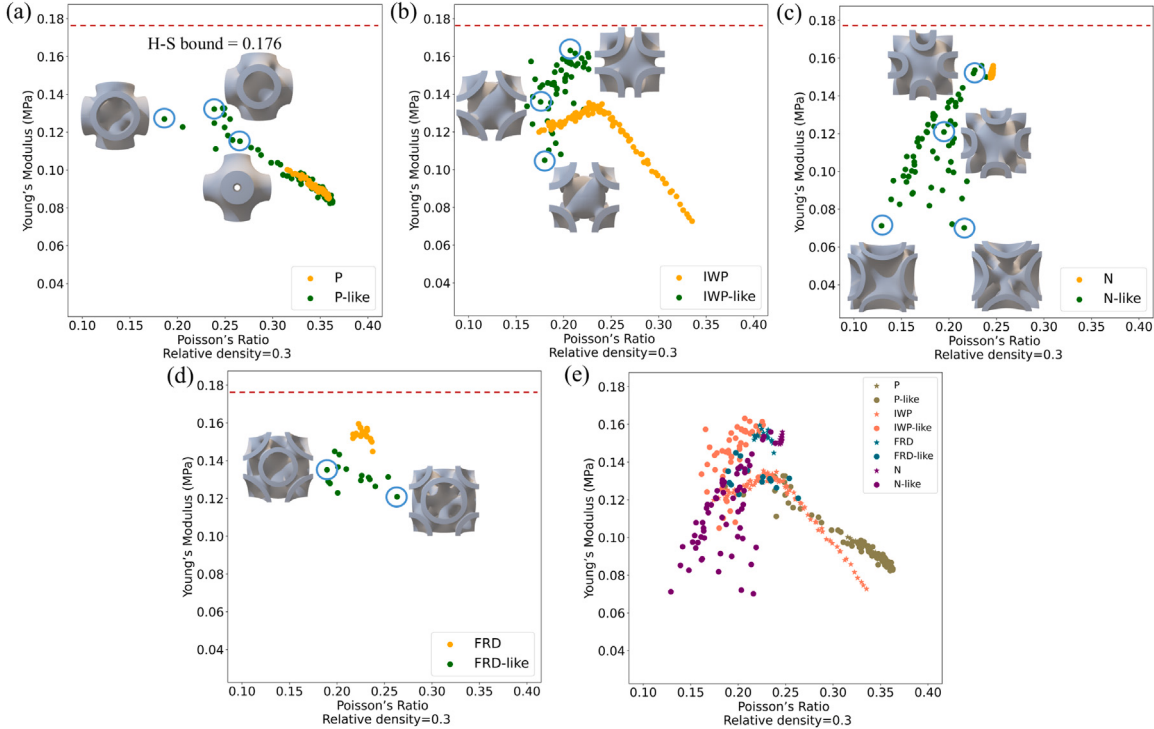


Fig. 12. The E - v space covered by our shell-lattices and TPMS-based shell-lattices.

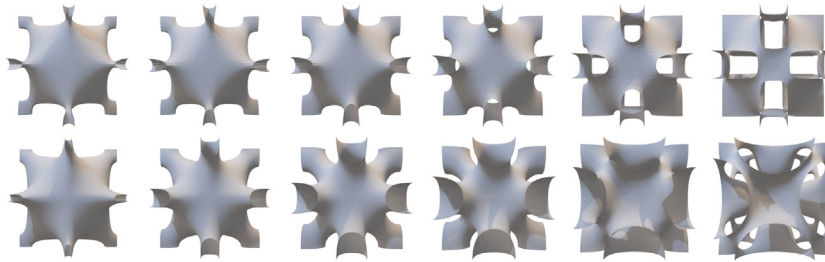


Fig. 13. Comparing samples generated with implicit methods and our method for N boundary topology. The first row is a group of N surfaces generated by varying the parameter c of implicit equations. The second row is a group of our N-like surfaces generated by varying the boundary parameters.

We also find that our P-like shell-lattices have better isotropic properties than P shell-lattices. Zener ratio is a standard metric to measure anisotropy properties. The closer the Zener ratio is to 1, the closer the structure is to be isotropic. We choose a surface that can be isotropic from our P-like family and choose $c = 0$ surface as the base surface with two iso-surfaces $c = \pm a$ for P shell-lattices. Different thickness and a values can generate P-like and P shell-lattices with different relative densities. The Young's modulus and Zener ratio with respect to relative density is demonstrated in Fig. 14 for P and P-like shell-lattices, which shows that our P-like shell-lattices have better isotropy than P shell-lattices and become isotropic at relative density 0.3. Further, our P-like shell-lattices have a larger Young's modulus when the relative density is

greater than 0.1. In comparison, it is difficult to achieve isotropy for the P shell-lattices by only changing c parameter at lower volume fractions. The Zener ratio of the P shell-lattices using different c parameters as base surface has been presented in [33]. To improve the isotropy for P shell-lattices, [30,33] combined P shell-lattices with other structures, and [34] enhanced isotropy via variable thickness design.

We also compare our TPMS-like surfaces with TPMS surfaces approximated by Eq. (1) in terms of mean curvature distributions. By definition, the mean curvature H should be zero everywhere on a minimal surface; we calculate it on discretized surface meshes according to [35] implemented by [36]. In Fig. 15 we show the mean curvature distribution for three types of TPMS and TPMS-like surfaces. The size

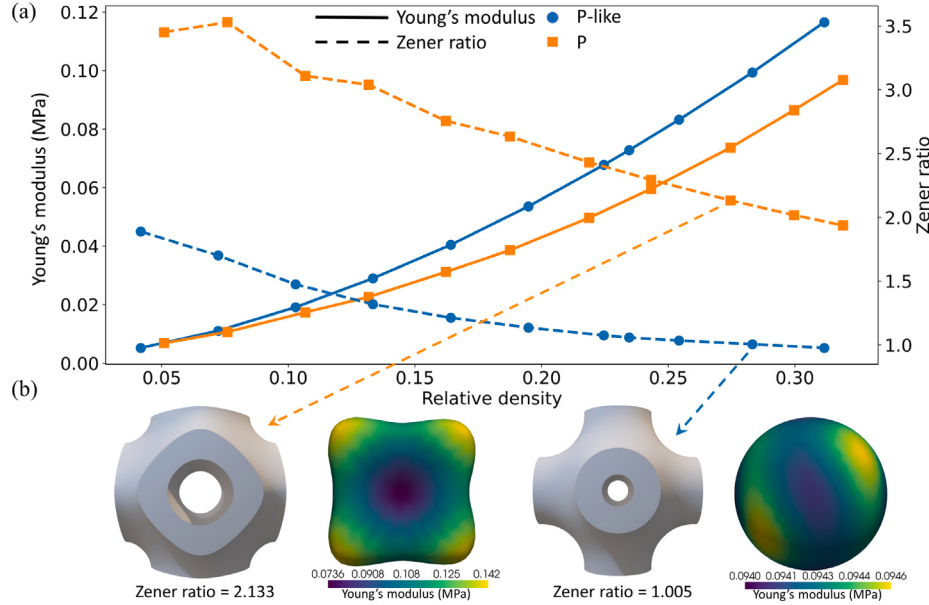


Fig. 14. (a) Young's modulus and Zener ratio versus relative density for P-like and P shell-lattices. (b) The surface of Young's modulus of P (left) and P-like (right) for the arrow points to the structure.

Type	P	P-like	IWP	IWP-like	N	N-like
Mean curvature						
Surface area(cm^2)	2.35	2.33	3.55	3.56	3.53	3.55
Vertices number	3192	3186	4822	4912	4678	4753
Faces number	6085	6042	9171	9307	8900	9037

Fig. 15. Comparison of the mean curvature H between TPMS and TPMS-like surfaces. Per-vertex curvatures are color-coded on the surfaces, and the distribution histograms of curvature values are shown below.

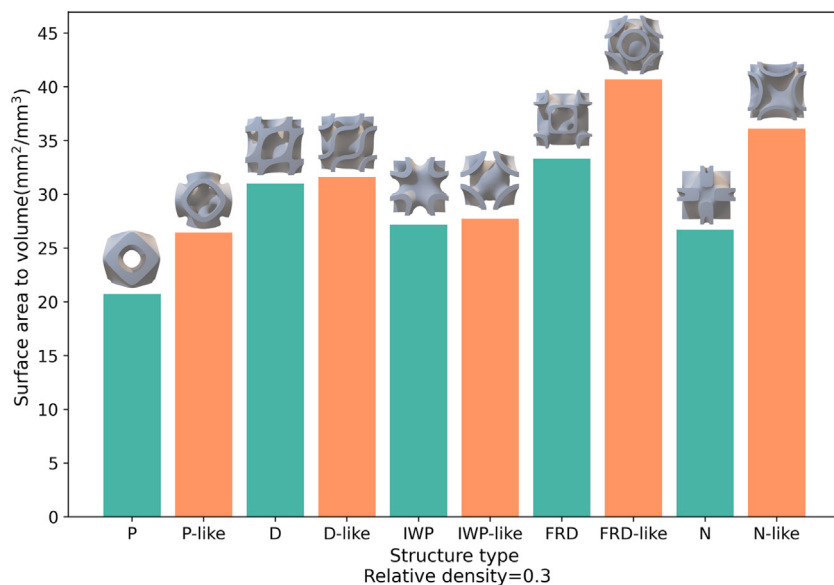


Fig. 16. The higher SA/V ratio of our shell-lattices and TPMS-based shell-lattices.

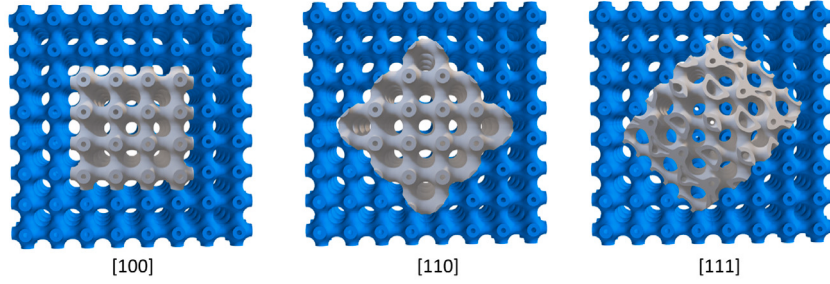


Fig. 17. Test specimens of our P-like structures along different directions.

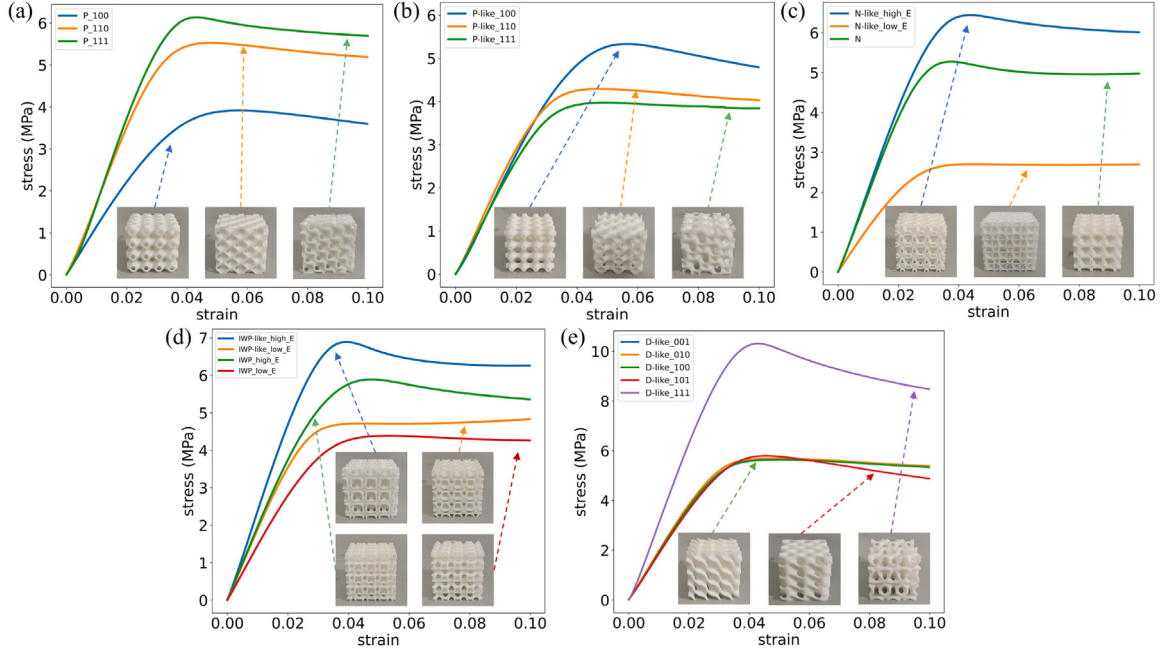


Fig. 18. The fabricated models and strain–stress curves.

of testing structures is $1 \times 1 \times 1$ cm. Overall, the mean curvatures of these surfaces are all close to zero, showing that our results are good approximations of TPMS structures. Specifically, the mean curvatures of P-like surface is more concentrated than that of the P surface, while the mean curvatures of N-like surface are slightly more spread out than N surface.

Finally, we analyzed the surface area to volume ratio (SA/V ratio) of these shell-lattices. This property is crucial for microstructures, especially for applications like biomimetic scaffolds and bioartificial tissues. For each group of shell-lattices we compared, we selected the shell-lattice with the higher SA/V ratio. The results, as depicted in Fig. 16, demonstrate that our P-like, FRD-like, and N-like shell-lattices have larger SA/V ratios when compared to the corresponding prior TPMS-based shell-lattices.

3.2. Experimental validation

In this section, we validate our computational results through experiments. We tested several of our shell structures with compression test, and compared the results to prior TPMS shell structures. We created specimens consisting of a grid of $4 \times 4 \times 4$ unit cells (40 mm×40 mm×40 mm) and fabricated by stereolithography technology with UV curable resin materials, as shown in Fig. 18. We perform five groups of compression tests on a universal testing machine (MTS Criterion44) and strain–stress responses were extracted and presented

in Fig. 18. The loading direction is consistent with the building direction of specimens in fabrication. Note that in this paper, we only examined the linear elastic properties of specimens. Evaluations on more deformation behaviors [37,38], are considered to be future work.

First, we validate whether our P-like shell structures have better isotropic properties. Uniaxial compression experiments are performed on two shell structures with similar relative density (about 27.7%) shown in Fig. 14. We obtained tested specimens that are oriented in the [100], [110], and [111] directions by intersecting the $8 \times 8 \times 8$ periodic structure and the cube along a specific orientation, as shown in Fig. 17. As anticipated, the strain–stress curve in Fig. 18(a) and (b) demonstrates that our P-like shell structure has a similar Young's modulus in all three directions, whereas the Young's modulus of the TPMS-P shell structure in three directions is distinct. In addition, the Young's modulus of the P-like shell structure is higher than that of the P shell structure in the [100] direction.

We then selected shell structures with the larger and the smaller Young's modulus from our N-like family and IWP-like family, and similarly with N and IWP shell structures. As demonstrated in (c) and (d) of Fig. 18, Young's modulus of $4 \times 4 \times 4$ N-like_high_E, N-like_low_E and N shell structures computed by homogenization with a resolution of $100 \times 100 \times 100$ are 0.157 MPa, 0.08 MPa, and 0.153 MPa, respectively, Young's modulus of $4 \times 4 \times 4$ IWP-like_high_E, IWP-like_low_E, IWP_high_E, and IWP_low_E are 0.166 MPa, 0.123 MPa, 0.123 MPa, and 0.1 MPa, respectively. The relative density of these structures ranged between 29.4% to 31.7%. The strain–stress curves

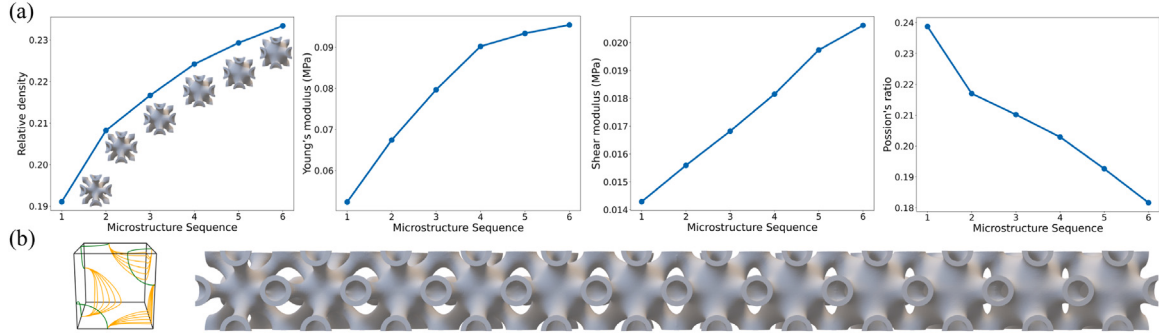


Fig. 19. Functionally graded design. (a) A collection of structures all sharing the boundary topology topo_1_rrr. From left to right, they exhibit variations in relative density, Young's modulus, shear modulus, and Poisson's ratio. (b) Left: variations in boundary geometry are presented, with the green color representing outer boundaries and the orange denoting inner boundaries post-synthesis. Right: a shell structure bar with functionally graded attributes and seamless connectivity.

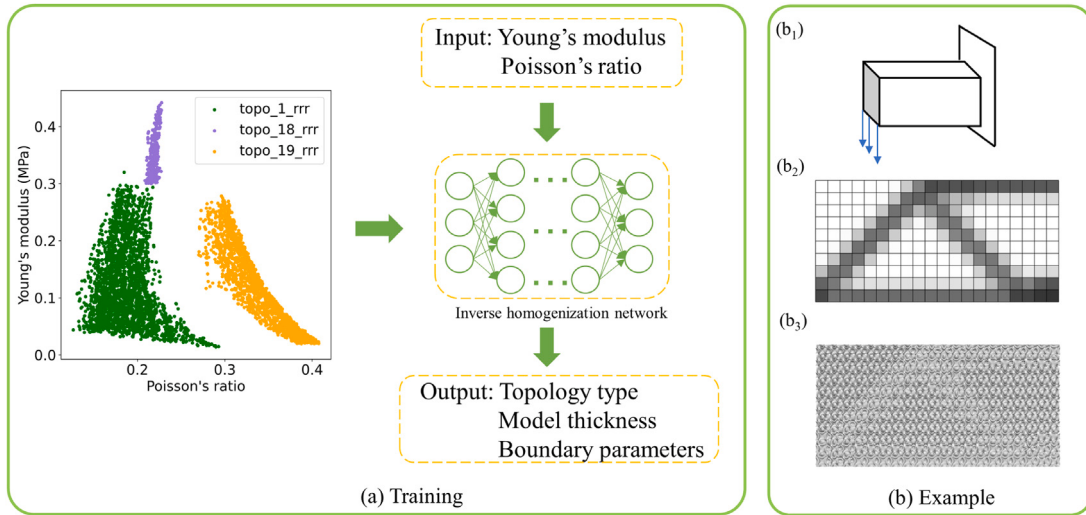


Fig. 20. (a) The data-driven pipeline for inverse homogenization. (b) A microstructural topological optimization example with inverse homogenization network: (b₁) The initial design domains of a cantilever beam. (b₂) The Young's modulus distribution of cantilever beam (grid 20 × 10 × 2) computed by [39]. (b₃) The cantilever beam model infilling according to our network prediction and Young's modulus distribution.

are consistent with the computational results of the homogenization method. The Young's modulus of N-like_high_E shell structure is similar to N shell structure and is much bigger than N-like_low_E shell structure. However, the minimum aperture of our N-like_high_E structure is much larger than that of N shell structure, which reduces the need for high-precision manufacturing techniques, as shown in the bottom of Fig. 18(c). The Young's modulus of our IWP-like_high_E shell and IWP-like_low_E shell structures is larger than that of IWP_high_E and IWP_low_E shell structures, respectively. For D-like shell structures, we conducted compression tests in the [001], [010], [100], [101], and [111] directions, and the strain-stress curve shown in Fig. 18(e) revealed that D-like shell structure has the same Young's modulus in [001], [010], [100], and [101] directions.

4. Applications

Our TPMS-like modeling approach can provide new choices for shell lattices in infill structure design. We discuss two potential applications of our framework on functionally graded materials design and inverse homogenization.

4.1. Functionally graded TPMS-like structures design

Functionally graded shell structures consist of microstructures with topologically similar forms but varying spatial properties. On a macro scale, these structures have the same topological form but different geometric parameters. However, designing functionally graded shell

structures typically involves complex topology optimization for the entire structure, which can be computationally expensive to ensure material connectivity and smoothly varying physical properties. Our proposed framework allows us to generate a group of unit cells with the same outer boundary but changing inner boundaries, resulting in functionally graded shell structures with perfect connections. In Fig. 19, we present an example where topo_1_rrr is employed to design a set of boundaries (as seen in Fig. 19(b) left). While these boundaries share the same outer boundary, they exhibit different inner boundaries upon being integrated into the unit-cell. It is important to emphasize that the validity of the functionally graded structures is ensured a posteriori. Specifically, if any structure exhibits irregularities, the sequence is interrupted. In Fig. 19, the composite boundary in the 1/8 cubic space, comprising both inner and outer contours, forms a closed loop, ensuring the integrity of the resultant structure.

4.2. Inverse homogenization of TPMS-like structures

While the proposed modeling framework enables us to create families of TPMS-like shell lattices with rich variations in both topology and geometry, the properties of generated structures can only be assessed posteriorly. To make the design of our structures more material property-oriented, we introduce an inverse homogenization method in this section. This method constructs a mapping from material properties to the shell structures and avoids the computationally expensive traditional method of solving it through topology optimization, which requires the computation of effective properties [40]. Instead,

we suggest using a data-driven model that learns the mapping and is implemented as a deep neural network.

The inverse design pipeline is shown in Fig. 20 left. In particular, based on the data-driven model introduced by [41], we train a conditional generative adversarial network (GAN) [42] to learn the mapping from material properties (E, v) to geometric parameters (Fig. 9) of our TPMS-like structures. We choose three topologies (topo_1_rrr, topo_18_rrr, topo_19_rrr) to generate our dataset. We generate samples of structures with random boundary parameters and surface thickness in an appropriate range. The collected dataset contains 5136 different shell structures for training and testing. More details are referred to Appendix.

In Fig. 20 (right), we present an example of microstructure topological optimization enabled by the inverse homogenization network. Following the methodology in [39], we implement topological optimization for a cantilever beam using a $20 \times 10 \times 2$ grid, as depicted in Fig. 20 (b₁). The resulting distribution of Young's modulus is displayed in Fig. 20 (b₂). In this particular example, we exclusively employ the N-like structures to train the inverse homogenization network, enabling us to predict the structural parameters associated with the desired Young's modulus distribution. Subsequently, we generate the corresponding N-like structures based on these predicted parameters and fill the beam, as shown in Fig. 20 (b₃). It is important to note that while this network predicts the properties of the structures, it does not guarantee the connectivity of all generated structures.

Besides the aforementioned applications, the proposed shell lattices form two independent connected spaces that can be filled with secondary or third materials to generate multi-functional properties such as enhanced toughness, high energy absorption, improved vibration and noise damping [2,43], and have also great potential in thermal and fluid flow systems.

5. Conclusion

Due to the excellent physical and geometric properties, TPMS-based shell-lattices have attracted a lot of research attention and have been widely fabricated in many artificial systems, given the advent of additive manufacturing. In most existing research, TPMSs are described by a limited set of mathematical expressions, and TPMS-based shell-lattices with different relative densities are obtained by only adjusting a single parameter. In order to exploit the structure and property space of shell-lattice metamaterials, in this work, we present a new framework to model richer families of TPMS-like shell structures, by parameterizing the topology and geometry of 1/8 cubical boundary conditions and constructing smooth minimal surfaces robustly.

To evaluate the properties of newly generated families of TPMS-like shell-lattices, we choose those with the same boundary conditions as prior TPMS-based shell-lattices, i.e., five classic structures (P, D, IWP, N, FRD), for comparison. Our computational results based on the homogenization method show that our TPMS-like shell-lattices cover a larger $E - v$ space, particularly for our N-like structures. Our P-like shell-lattices can achieve elastic isotropy. The surface area to volume ratio of our P-like, FRD-like, and N-like shell-lattices are larger than corresponding prior TPMS-based shell-lattices. In addition, we show two applications about functionally graded design and inverse design which are enabled by our modeling framework.

There are numerous intriguing avenues for future research. For instance, although we have utilized 1/8 cubes, degenerate surfaces can still arise when solving minimal surfaces for multiple closed boundary conditions. This limitation reduces the design space available for our shell-lattices. To overcome this challenge, it may be worthwhile to explore the use of even smaller units, allowing for more diverse compositions and further enriching the families of complex TPMS-like shell lattices.

Another aspect to consider is the impact of setting a large thickness parameter to obtain structures with a high volume fraction. This can

result in reduced smoothness and even self-crossing due to intricate topology, such as our FRD-like structures. To address these issues, future research could focus on generating structures with non-uniform thickness. This approach has the potential to improve smoothness and mitigate self-crossing problems.

Moreover, a detailed exploration of the properties exhibited by the more exotic and anisotropic structures we have generated would be valuable. Additionally, investigating their inverse design using suitable deep neural network architectures holds promise for further advancement.

Lastly, conditioned inverse design, incorporating additional constraints such as specified outer boundaries, presents an interesting area for exploration. This approach involves designing structures while satisfying specific constraints, offering intriguing possibilities for future investigations.

CRediT authorship contribution statement

Yonglai Xu: Writing – original draft, Software, Methodology, Investigation. **Hao Pan:** Writing – review & editing, Supervision, Methodology, Investigation. **Ruonan Wang:** Validation, Investigation. **Qiang Du:** Writing – review & editing, Supervision. **Lin Lu:** Writing – review & editing, Supervision, Resources, Funding acquisition, Conceptualization.

Declaration of competing interest

The authors declare that they have no known competing financial interests or personal relationships that could have appeared to influence the work reported in this paper.

Data availability

Data will be made available on request.

Acknowledgments

We thank all the anonymous reviewers for their valuable comments and constructive suggestions. This work is supported by the grant No. 61972232 from National Natural Science Foundation of China (NSFC), No. CJGJZD20200617102202007 from Science, Technology and Innovation Commission of Shenzhen Municipality, China.

Appendix. Details of inverse homogenization of TPMS-like structures

The objective of inverse homogenization design is building the mapping from material properties (Young's modulus E , Poisson's ratio v) to geometrical parameters (position, derivative, and thickness) of our TPMS-like structures. In [41], they generate the composite TPMS structures by mixing three TPMS implicit equations. The composite TPMS structures can be represented as three mixing weights and three level-set values. They use a conditional generative adversarial network (GAN) [42] to perform inverse design by learning the mapping from the property space to the shape parameter space. Motivated by their work, we also use a conditional GAN model to learn this mapping, and the shape parameter space is defined by the geometrical parameters of our TPMS-like structures. Given the condition of material properties, the conditional GAN can generate multiple structures that satisfy targeted material properties by sampling noise vectors from a predefined prior distribution. The conditional GAN architecture includes the generative model G , the discriminative model D , and the auxiliary property regressor R , which are fully-connected neural networks (Fig. A.21). The input of generator G are specific material properties and noise vector z , predefined prior distribution P_z . The auxiliary property regressor R

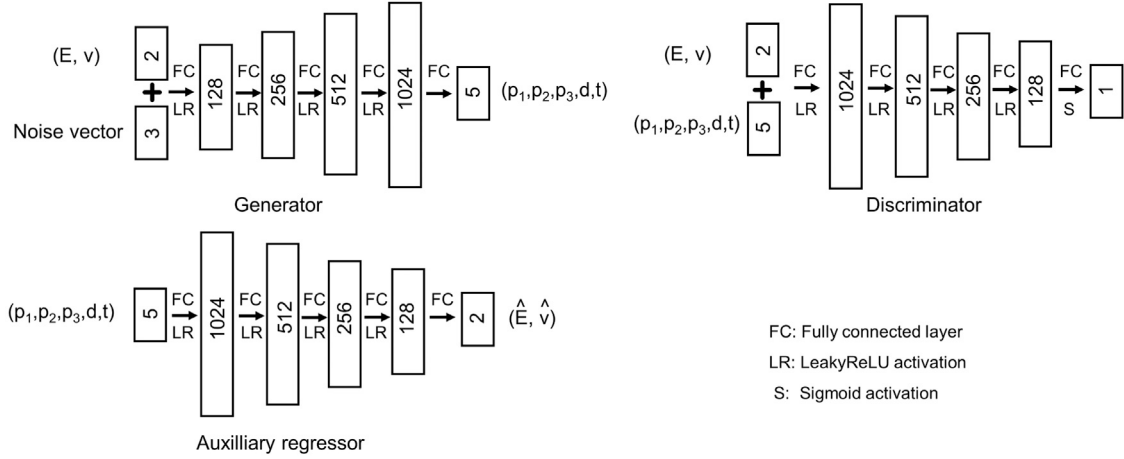


Fig. A.21. Neural network architectures used for inverse design.

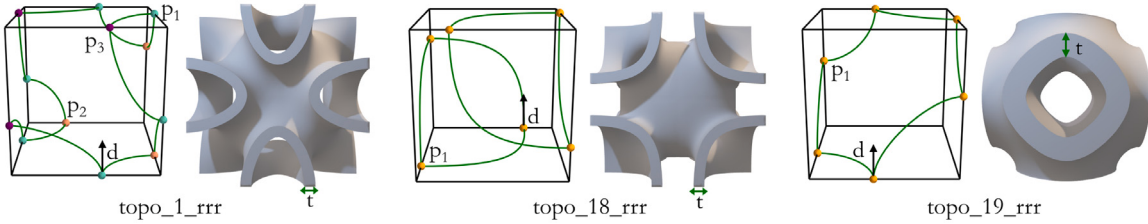
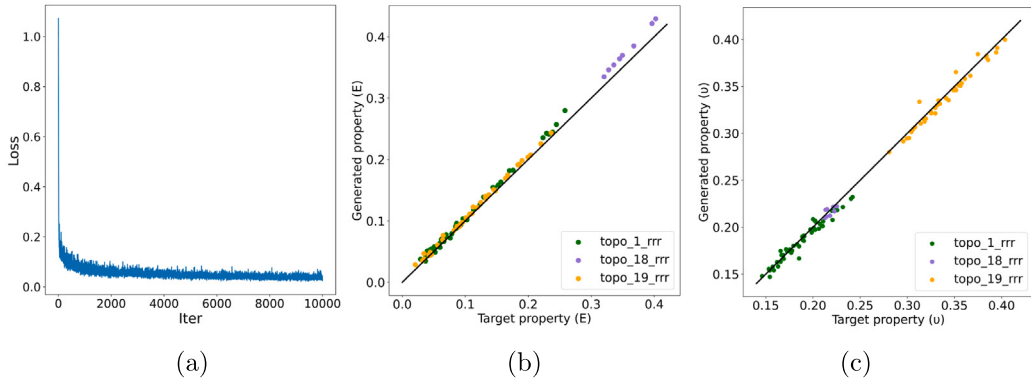


Fig. A.22. The parametric representation of topo_1_rrr, topo_18_rrr, topo_19_rrr with cubic symmetric geometry.

Fig. A.23. The loss function curve of cGAN (a) and the property prediction error of E (b) and v (c) for the test dataset.

is to improve accuracy when mapping back to material properties. The loss function of conditional GAN is:

$$\begin{aligned} \min_{G,R} \max_D V_{\text{cGAN}}(D, G, R) = & \mathbb{E}_{x \sim P_{\text{data}}} [\log D(x | y)] \\ & + \mathbb{E}_{z \sim P_z} [\log (1 - D(G(z | y)))] \\ & + \lambda (\mathbb{E}_{z \sim P_z} [|y - R(G(z | y))|]) \\ & + \mathbb{E}_{x \sim P_{\text{data}}} [|y - R(x)|] \end{aligned} \quad (\text{A.1})$$

where x means geometrical parameters of the TPMS-like structures and $y = (E, v)$ in our work.

We choose three topologies (topo_1_rrr, topo_18_rrr, topo_19_rrr) to generate our dataset. To simplify the representation of parameters, we generate TPMS-like structures with cubic symmetric geometry. Three structures can be represented as (p_1, p_2, p_3, d, t) , (p_1, d, t) , (p_1, d, t) , separately as shown in Fig. A.22. Then we randomly sample in an appropriate range (Table A.1) for the position, derivative, and thickness parameters to avoid disconnectivity and solid space

issues. To classify the topology type of the geometric parameters predicted by the network, we add two additional position parameters for topo_18_rrr and topo_19_rrr, and their values are uniformly set outside the position range of topo_1_rrr. After removing overlaps in E - v space between different topologies, the final dataset comprises 5136 unit cells, including 2906 topo_1_rrr unit cells, 298 topo_18_rrr unit cells, and 1932 topo_19_rrr unit cells. This dataset is divided into 5036 samples for training and 100 samples (consisting of 50 topo_1_rrr unit cells, 10 topo_18_rrr unit cells, and 40 topo_19_rrr unit cells) for evaluation purposes.

We train this cGAN for 10^5 iterations (2.6 min on a GeForce GTX TITAN Xp) with a learning rate of 0.0002 and randomly sample 32 examples as a mini-batch for each iteration. The hyperparameter λ is set to 20 in the loss function. To evaluate the precision of this conditional GAN, we compute the property prediction error on the test dataset

Table A.1

We set our 1/8 design space as a $2 \times 2 \times 2$ mm cube. This table shows the appropriate geometrical parameters range for position, derivative, and thickness.

Parameter	Type	topo_1_rrr	topo_18_rrr	topo_19_rrr
Position (mm)		$p_1, p_2, p_3: [-0.45, 0.45]$	$p_1: [0.45, 0.8], p_2 = p_3 = -1$	$p_1: [-0.4, 0.4], p_2 = p_3 = 1$
Derivative		[1.0, 2.0]	[2.0, 4.0]	[1.0, 2.0]
Thickness (mm)		[0.1, 0.3]	[0.1, 0.4]	[0.1, 0.5]

using the coefficient of determination (R^2 -score):

$$R^2 = 1 - \frac{\sum_{i=1}^N \|y_i - \bar{y}_i\|^2}{\sum_{i=1}^N \|y_i - \bar{y}_i\|^2} \quad (\text{A.2})$$

where y_i means the target material properties, \bar{y}_i means the mean of the target material properties, and y'_i means the actual material properties of structures generated by the predicted geometrical parameters. The loss function curve of cGAN is shown in Fig. A.23(a). Removing some self-intersecting models, the property prediction error of the test dataset are shown in Fig. A.23(b)(c). The R^2 -score of E and v property are 0.9906 and 0.9943, respectively.

References

- [1] L. Lu, A. Sharf, H. Zhao, Y. Wei, Q. Fan, X. Chen, Y. Savoye, C. Tu, D. Cohen-Or, B. Chen, Build-to-last, ACM Trans. Grap. 33 (4) (2014) 1–10, <http://dx.doi.org/10.1145/2601097.2601168>.
- [2] X. Yan, C. Rao, L. Lu, A. Sharf, H. Zhao, B. Chen, Strong 3D printing by TPMS injection, IEEE Trans. Visual. Comput. Grap. 26 (10) (2020) 3037–3050, <http://dx.doi.org/10.1109/tvcg.2019.2914044>.
- [3] M.G. Lee, J.W. Lee, S.C. Han, K. Kang, Mechanical analyses of Shellular, an ultralow-density material, Acta Mater. 103 (2016) 595–607, <http://dx.doi.org/10.1016/j.actamat.2015.10.040>.
- [4] O. Al-Ketan, R. Rowshan, R.K.A. Al-Rub, Topology-mechanical property relationship of 3D printed strut, skeletal, and sheet based periodic metallic cellular materials, Addit. Manuf. 19 (2018) 167–183, <http://dx.doi.org/10.1016/j.addma.2017.12.006>.
- [5] T. Tancogne-Dejean, M. Diamantopoulou, M.B. Gorji, C. Bonatti, D. Mohr, 3D plate-lattices: An emerging class of low-density metamaterial exhibiting optimal isotropic stiffness, Adv. Mater. 30 (45) (2018) 1803334, <http://dx.doi.org/10.1002/adma.201803334>.
- [6] W. Li, G. Yu, Z. Yu, Bioinspired heat exchangers based on triply periodic minimal surfaces for supercritical CO₂ cycles, Appl. Therm. Eng. 179 (2020) 115686, <http://dx.doi.org/10.1016/j.applthermaleng.2020.115686>.
- [7] J. Kim, D.-J. Yoo, 3D printed compact heat exchangers with mathematically defined core structures, J. Comput. Des. Eng. 7 (4) (2020) 527–550, <http://dx.doi.org/10.1093/jcde/qwaa032>.
- [8] X.-Y. Zhang, X.-C. Yan, G. Fang, M. Liu, Biomechanical influence of structural variation strategies on functionally graded scaffolds constructed with triply periodic minimal surface, Addit. Manuf. 32 (2020) 101015, <http://dx.doi.org/10.1016/j.addma.2019.101015>.
- [9] J. Feng, J. Fu, C. Shang, Z. Lin, X. Niu, B. Li, Efficient generation strategy for hierarchical porous scaffolds with freeform external geometries, Addit. Manuf. 31 (2020) 100943, <http://dx.doi.org/10.1016/j.addma.2019.100943>.
- [10] Y. Jin, S. Zou, B. Pan, G. Li, L. Shao, J. Du, Biomechanical properties of cylindrical and twisted triply periodic minimal surface scaffolds fabricated by laser powder bed fusion, Addit. Manuf. 56 (2022) 102899, <http://dx.doi.org/10.1016/j.addma.2022.102899>.
- [11] W. Yang, J. An, C.K. Chua, K. Zhou, Acoustic absorptions of multifunctional polymeric cellular structures based on triply periodic minimal surfaces fabricated by stereolithography, Virtual Phys. Prototyp. 15 (2) (2020) 242–249, <http://dx.doi.org/10.1080/17452759.2020.1740747>.
- [12] T. Femmer, A.J. Kuehne, J. Torres-Rendon, A. Walther, M. Wessling, Print your membrane: Rapid prototyping of complex 3D-PDMS membranes via a sacrificial resist, J. Membr. Sci. 478 (2015) 12–18, <http://dx.doi.org/10.1016/j.memsci.2014.12.040>.
- [13] S. Torquato, A. Donev, Minimal surfaces and multifunctionality, Proc. R. Soc. Lond. Ser. A Math. Phys. Eng. Sci. 460 (2004) 1849–1856, <http://dx.doi.org/10.1098/rspa.2003.1269>.
- [14] Z. Gan, M.D. Turner, M. Gu, Biomimetic gyroid nanostructures exceeding their natural origins, Sci. Adv. 2 (5) (2016) <http://dx.doi.org/10.1126/sciadv.1600084>.
- [15] L. Han, S. Che, An overview of materials with triply periodic minimal surfaces and related geometry: From biological structures to self-assembled systems, Adv. Mater. 30 (17) (2018) 1705708, <http://dx.doi.org/10.1002/adma.201705708>.
- [16] W.E. Lorensen, H.E. Cline, Marching cubes: A high resolution 3D surface construction algorithm, ACM SIGGRAPH Comput. Grap. (1987) 163–169.
- [17] H.A. Schwarz, Gesammelte Mathematische Abhandlungen: Second Edition, Second Ed., Gesammelte mathematische Abhandlungen, 1970.
- [18] A.H. Schoen, Infinite Periodic Minimal Surfaces Without Self-Intersections, Tech. rep., NASA Electronics Research Center Cambridge, MA, United States, 1970.
- [19] W. Fischer, E. Koch, On 3-periodic minimal surfaces, Zeitschrift für Kristallographie - Crystalline Materials 179 (1–4) (1987).
- [20] H. Karcher, K. Polthier, Construction of triply periodic minimal surfaces, Phil. Trans. R. Soc. A 354 (1715) (1996).
- [21] S. Wang, A. Chern, Computing minimal surfaces with differential forms, ACM Trans. Graph. 40 (4) (2021).
- [22] D. Palmer, D. Smirnov, S. Wang, A. Chern, J. Solomon, DeepCurrents: Learning implicit representations of shapes with boundaries, in: Proceedings of the IEEE/CVF Conference on Computer Vision and Pattern Recognition, CVPR, 2022.
- [23] R. Diestel, Graph Theory, Springer Berlin Heidelberg, 2017.
- [24] F. Dunn, I. Parberry, 3D Math Primer for Graphics and Game Development, Taylor & Francis Inc, 2011.
- [25] N. Pipenbrinck, Hermite curve interpolation, 1998, URL <https://www.cubic.org/docs/hermite.htm>.
- [26] J.F. Nye, Physical Properties of Crystals: Their Representation By Tensors and Matrices, Oxford University Press, 1985.
- [27] H. Peng, A. Liu, J. Huang, L. Cao, J. Liu, L. Lu, PH-net: Parallelepiped microstructure homogenization via 3D convolutional neural networks, Addit. Manuf. 60 (2022) 103237, <http://dx.doi.org/10.1016/j.addma.2022.103237>.
- [28] S. Rastegarzadeh, J. Wang, J. Huang, Two-scale topology optimization with isotropic and orthotropic microstructures, Designs 6 (5) (2022) 73, <http://dx.doi.org/10.3390/designs06050073>.
- [29] P. Liu, A. Liu, H. Peng, L. Tian, J. Liu, L. Lu, Mechanical property profiles of microstructures via asymptotic homogenization, Comput. Grap. 100 (2021).
- [30] Z. Chen, Y.M. Xie, X. Wu, Z. Wang, Q. Li, S. Zhou, On hybrid cellular materials based on triply periodic minimal surfaces with extreme mechanical properties, Mater. Des. 183 (2019) 108109, <http://dx.doi.org/10.1016/j.matdes.2019.108109>.
- [31] P. Liu, B. Sun, J. Liu, L. Lu, Parametric shell lattice with tailored mechanical properties, Addit. Manuf. 60 (2022) 103258, <http://dx.doi.org/10.1016/j.addma.2022.103258>.
- [32] J.B. Berger, H.N.G. Wadley, R.M. McMeeking, Mechanical metamaterials at the theoretical limit of isotropic elastic stiffness, Nature 543 (7646) (2017) 533–537, <http://dx.doi.org/10.1038/nature21075>.
- [33] J. Feng, B. Liu, Z. Lin, J. Fu, Isotropic porous structure design methods based on triply periodic minimal surfaces, Mater. Des. 210 (2021) 110050, <http://dx.doi.org/10.1016/j.matdes.2021.110050>.
- [34] Q. Ma, L. Zhang, J. Ding, S. Qu, J. Fu, M. Zhou, M.W. Fu, X. Song, M.Y. Wang, Elastically-isotropic open-cell minimal surface shell lattices with superior stiffness via variable thickness design, Addit. Manuf. 47 (2021) 102293, <http://dx.doi.org/10.1016/j.addma.2021.102293>.
- [35] D. Cohen-Steiner, J.-M. Morvan, Restricted delaunay triangulations and normal cycle, in: Proceedings of the Nineteenth Annual Symposium on Computational Geometry, SCG '03, Association for Computing Machinery, 2003, pp. 312–321.
- [36] Gabriel Peyré, Toolbox graph, 2023, URL <https://www.mathworks.com/matlabcentral/fileexchange/5355-toolbox-graph>.
- [37] C. Bhat, A. Kumar, S.-C. Lin, J.-Y. Jeng, Design, fabrication, and properties evaluation of novel nested lattice structures, Addit. Manuf. 68 (2023) 103510, <http://dx.doi.org/10.1016/j.addma.2023.103510>.
- [38] B. Sun, X. Yan, P. Liu, Y. Xia, L. Lu, Parametric plate lattices: Modeling and optimization of plate lattices with superior mechanical properties, Addit. Manuf. 72 (2023) 103626, <http://dx.doi.org/10.1016/j.addma.2023.103626>.
- [39] K. Liu, A. Tovar, An efficient 3D topology optimization code written in matlab, Struct. Multidiscip. Optim. 50 (6) (2014) 1175–1196, <http://dx.doi.org/10.1007/s00158-014-1107-x>.
- [40] S. Kumar, S. Tan, L. Zheng, D.M. Kochmann, Inverse-designed spinodoid meta-materials, npj Comput. Mater. 6 (1) (2020) <http://dx.doi.org/10.1038/s41524-020-0341-6>.
- [41] J. Wang, W.W. Chen, D. Da, M. Fuge, R. Rai, IH-GAN: A conditional generative model for implicit surface-based inverse design of cellular structures, Comput. Methods Appl. Mech. Engrg. 396 (2022) 115060, <http://dx.doi.org/10.1016/j.cma.2022.115060>.
- [42] M. Mirza, S. Osindero, Conditional generative adversarial nets, 2014, arXiv: 1411.1784.
- [43] M.J. Prajapati, C. Bhat, A. Kumar, S. Verma, S.-C. Lin, J.-Y. Jeng, Supportless lattice structure for additive manufacturing of functional products and the evaluation of its mechanical property at variable strain rates, Materials 15 (22) (2022) <http://dx.doi.org/10.3390/ma15227954>.